Contents lists available at SciVerse ScienceDirect

CIRP Annals Manufacturing Technology

Journal homepage: www.elsevier.com/locate/cirp

The role of scan strategies in fatigue performance for laser powder bed fusion

Wessel W. Wits[1,2] (2), Enrico Scolaro[3], Emiel Amsterdam[3] and Adam T. Clare[4] (2)

[1]*Mechanical & Electrical Engineering Department, Thales Nederland B.V., Hengelo, Netherlands*
[2]*Faculty of Electrical Engineering, Mathematics and Computer Science, University of Twente, Enschede, Netherlands*
[3]*NLR – Royal Netherlands Aerospace Centre, Marknesse, Netherlands*
[4]*Faculty of Engineering, University of Nottingham, Nottingham, UK*

The integrity of additively manufactured components is limited by the number, size, type and location of defects encapsulated in the build. Our ability to manufacture fatigue resistant components by the powder bed fusion process is still nascent as a result. The location of defects within a build volume is known to be of significance but efforts are yet to achieve superior manufacturing strategies resulting in tolerable fatigue performance. In this work the role of laser scan strategies is investigated in determining fatigue performance of printed components. Fractography and X-ray computed tomography data are presented to support this.

Additive Manufacturing, Fatigue, Laser powder bed fusion

1. Introduction

Additive Manufacturing (AM) provides well understood design freedoms to industrial users; however, the uptake of AM for cyclically loaded components is modest. This is due, in part, to functional performance of AM components in fatigue. The relationship of fatigue performance to manufacturing processes has been well reported in literature [1]. Understanding defect formation and detecting these in AM has also been widely explored in literature and extensive resources are now available to metal AM practitioners seeking to improve part integrity [2]. Despite this, practical suggestions for improving part integrity at the scan strategy level of production are yet to be elucidated.

The industrial application of X-ray Computed Tomography (XCT) is rapidly increasing [3]. To evaluate the level of defects within Laser Powder Bed Fusion (LPBF), Maskery et al. explored the use XCT and proposed a workflow to allow segmentation of pore sizes [4]. The use of XCT for characterisation of metal AM parts has gone on to attract significant research interest [5], but analysis of LPBF components is hampered by the native resolution of this technique. Commercially available XCT apparatus is typically only able to detect voids >10 µm. As a result a significant proportion of the defect population (including gas pores), which may be <2 µm, will not be detected. With current class LPBF technologies some level of porosity, regarded as important quality indicator in metal AM [6], is hence unavoidable.

Post processing may be undertaken to negate the effects of defects within AM components. Hot Isostatic Pressing (HIP) has been reported as a means by which to enhance the integrity of components by partially sealing micro pores and cracks [7]. As a result, tensile strength and elongation to failure have been enhanced and mechanical properties approach that of wrought equivalents. It is also possible to enhance the surface integrity of components by secondary processing such as shot peening [8], but this serves to undermine the primary case for using AM in that manufacturing chains become more contrived and therefore more costly. Where possible, near net geometry and material properties should be achieved in the initial build process.

Mechanical properties of AM components are, in part, set by AM process characteristics such as thermal history (i.e. melt pool temperature, cooling rate, etc.) affecting the microstructure [9]. When considering heat-treated and post-process machined components, defects serving as crack initiation sites are the main contributor affecting fatigue performance [10]. In LPBF, generally two types of defect are distinguished: i) entrapped gas due to vapour recoil during melt pool formation also known as keyholing and ii) lack of fusion caused by insufficient laser penetration or energy. Entrapped gas bubbles are typically spherical and small in size, while lack-of-fusion defects are irregularly shaped and often still include partially- or unmolten powder particles [4, 7, 11].

Surface properties of AM components and hence the laser 'skin scan strategy' creating the contour in the *x-y* plane (*see* Figure 1 for convention) is of critical importance in AM part design. Beevers et al. showed that test specimens without skin (contour) scanning have a longer fatigue life than specimens fabricated with a skin pass, due to the inter-track defects created [12]. With current industrial AM capabilities, post-process machining is inevitable for cyclically loaded components. This provides an opportunity to enhance the near surface of components by modifying the scan strategy which will be subject to machining. Critical to understand is the impact of machine path planning to the laser scan strategy. In this study, skin pass strategies are modified alongside hatch scan parameters of inner regions in order to understand the role of these in curtailing part fatigue life.

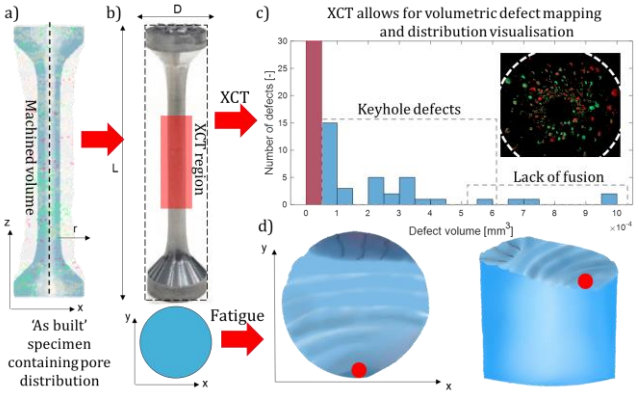

Figure 1. Specimen blanks (a-b) fabricated using various scan strategies exhibit distinct pore distributions revealed by XCT of the gauge section (c). These can be mapped in a facile manner and principle failure defects following fatigue testing can be identified through fractography (d).

2. Methodology

In order to evaluate the fatigue response to various skin and hatch scan strategies, six specimen types were manufactured. The types were designed to intentionally contain common LPBF defects with various shapes and sizes at various locations. The approach taken in this work is illustrated in Figure 1. Specimens were manufactured by LPBF using an SLM Solutions 280HL system and AlSi10Mg as feedstock material. Cylindrical test specimens were printed in the vertical build direction with, at the gauge section, a diameter and length of Ø4 and 18 mm, respectively. All builds went through a stress relieve heat treatment (2h at 300°C) after which the test specimens were machined and polished to the final gauge diameter of Ø3 mm (*see* Figure 1(b)) in accordance with ASTM test method E466-96. The as-built condition was not examined, as in that case surface effects would dominate the results rather than the scan strategy.

The scan strategies applied for building the six specimen types are depicted in Figure 2 and LPBF process parameters are listed in Table 1. Specimen type A is built using the material specific optimized parameter set, which was derived in an earlier test campaign that focused on minimizing porosity. During machining to Ø3 mm, the outer two skin passes are removed leaving only hatch defects present in the specimen. Contour region defects (type B) are simulated by printing a pattern of six consecutive skin passes at a slightly higher energy density and afterwards machining away the outer three passes. Defects at the surface and sub-surface (types C & D) are simulated similarly; however, with less skin passes and at an even higher energy density. After machining, the surface and sub-surface defect specimens contain a single and two skin passes, respectively. In these four types, the hatch scan parameter set is similar and equal to the optimized set. The skin pass spacing is set to 0.165 mm and the skin-hatch offset is zero. Between layers a 67° rotation of the hatch scan strategy is applied. Finally, keyhole defects (i.e. entrapped gas bubbles) in the core of a part were synthesized by increasing the energy density of the hatch parameter set by 25% (low) and 37% (high) compared to the optimized level. Also, for specimen type E the hatch spacing is reduced from 0.13 mm to 0.11 mm to increase the energy density.

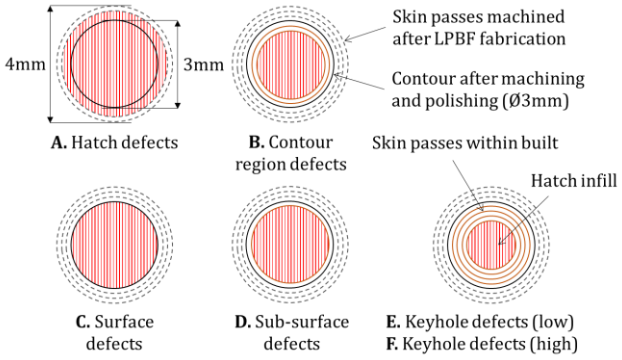

Figure 2. Six intentionally designed defects within the gauge section of test specimens subjected to fatigue testing.

In total, 78 test specimens, 13 of each type, were fabricated in three consecutive builds. Of each specimen type, one specimen was comprehensively analysed by XCT using a YXLON Cheetah EVO system and ImageJ as analysis software [13]. The system had a 16-bit detector with 1004x1004 pixels and scans were conducted using 715 projections with tube voltage 80 kV, current 11 µA and exposure time 3 s. The 12 mm gauge length of the specimens, as indicated by the XCT region in Figure 1(b), was scanned at a pixel resolution of 11.8 µm.

The acquired datasets were binarized by greyscale thresholding and detected voids below $5{\cdot}10^{-5}$ mm^3 were rejected as noise (*see* Figure 1(c)). Hence, spherical (gas) bubbles, as well as irregular lack-of-fusion voids across at least two layers, with a length scale of at least four pixels, i.e. ~50 µm, are classified as porosity. The defect size is characterized by the Feret diameter, a measure for a pore's maximum calliper size. The Feret diameter was determined for each detected pore and used to analyse the pore size distribution. Also, the pore locations were mapped as a function of the radial distance and used to visualize the pore distribution (*see* '*z*' projection inset of Figure 1(c)).

Table 1. Summary of LPBF process parameters used to create the six specimen types with intentional defects subjected to fatigue testing.

Specimen type	Skin parameters (power, speed, density, no. of passes)	Hatch parameters (power, speed, density, spacing)
A. Hatch defects	189 W, 677 mm/s, 0.279 J/mm, 2	380 W, 1306 mm/s, 0.291 J/mm, 0.13 mm
B. Contour region defects	200 W, 677 mm/s, 0.295 J/mm, 6	
C. Surface defects	230 W, 677 mm/s, 0.340 J/mm, 4	
D. Sub-surface defects	230 W, 677 mm/s, 0.340 J/mm, 5	
E. Keyhole defects (low)	230 W, 677 mm/s, 0.340 J/mm, 8	380 W, 1047 mm/s, 0.363 J/mm, 0.11 mm
F. Keyhole defects (high)		350 W, 875 mm/s, 0.400 J/mm, 0.13 mm

All 78 test specimens were fatigue tested by force controlled constant amplitude axial loading on a Schenck fatigue test rig. In order to reach at least 50,000 cycles, an initial trial was conducted on specimen types B, C & F, as these were assumed to fail at the lowest number of cycles. An appropriate maximum stress level was determined to be 140 MPa. At least nine test specimens of each type were fatigue tested at this stress level.

After failure, each specimen was further examined. Optical microscopy was used to observe the fracture surface and analyse the most significant defect size and position. The defect size was determined by the major axis of the defect. The position was recorded as the minimum distance from the defect edge to the specimen's outer surface. Fractures stemming from the outer surface are classified as surface defects, while internal defects are labelled as sub-surface defects.

3. Results and discussion

3.1. Relating XCT evaluation to LPBF build strategy

Figure 3 shows the Feret diameter as a function of the radial position of the defect. The insets show the '*z*' projections in which all defects are superimposed along the specimen's principle axis to a single plane. With 149 detected defects, specimen type A shows the lowest number of defects. Also, with an average defect size and volume of 79 µm and $7.1{\cdot}10^{-5}$ mm^3, respectively, defects are the smallest of the six types. Although the hatch scan pattern is similar across the *x-y* plane, most defects are located near the specimen's edge. This may be attributed to the fact that these locations are closer to the laser turn point at which location the process may enter into a keyhole regime generating pore defects [14]. For specimen type A, the laser turn points fall outside the machined contour, while for the other specimen types regions where the hatch scan pattern meets the skin pass are within the contour and hence show a higher number of defects.

For specimen type B, most defects are observed in the outer 0.5 mm of the specimen at the position where the adjacent skin passes reside. With a largest Feret diameter of 729 µm, this specimen type shows the largest defect size. The average defect volume of $2.7{\cdot}10^{-4}$ mm^3 is also the largest of the six specimen types. These large defects are an indication of the (intentionally

designed) lack-of-fusion defects originating between the skin passes, which was also confirmed by 3D XCT image analysis showing highly irregular defects.

Specimen types C & D show a dense region of defects at the location where the skin pass meets the hatch pattern. For specimen type C, most defects are close to the specimen edge, as the aim was to create surface-breaking defects. For specimen type D the denser region is a little more inward synthesizing sub-surface defects, as intended. Specimen type C has a higher pore count, as well as a higher average defect size and volume compared to specimen type D. By analysing 3D XCT visualizations, most pores are spherical in nature; hence, most defects are associated with keyhole defects likely due to the aforementioned laser turn point between skin and hatch passes.

As expected, specimen types E & F show a large number of defects across the entire cross section. The average defect size and volume are similar to the specimen type A, only the pore count is much higher. For specimen type F, the region of the hatch scan pattern shows less defects, but larger average defect sizes and volumes. Here, the higher energy density is assumed to have created less, but larger entrapped gas bubbles due to the keyholing effect.

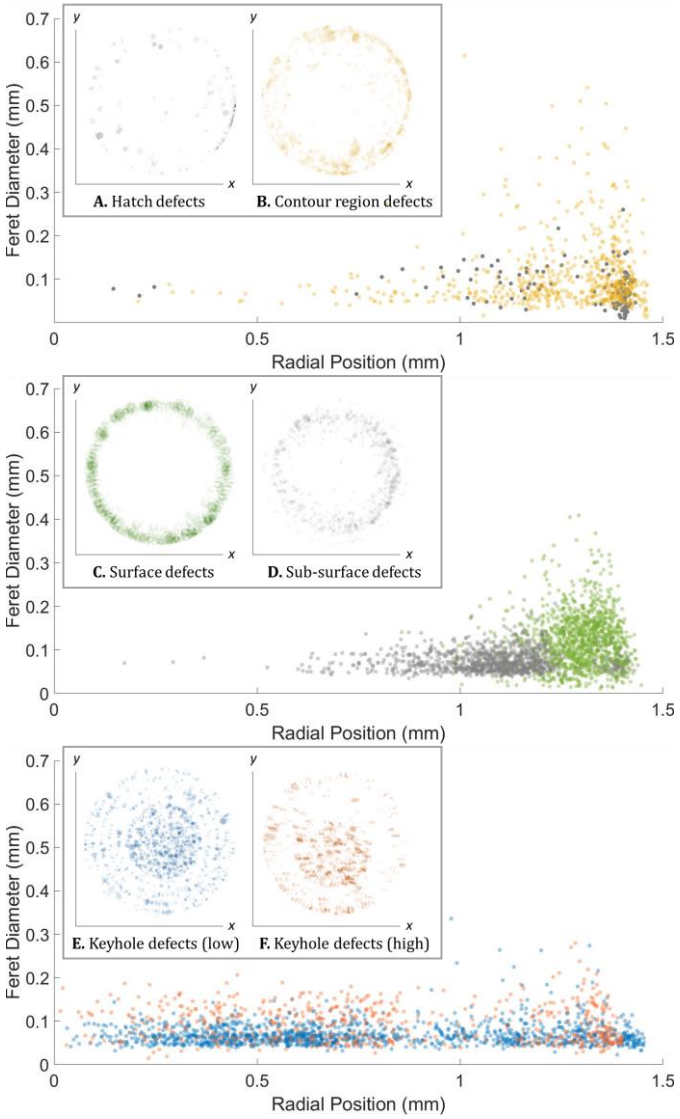

Figure 3. Plots of defect size (Feret diameter) against radial position correspond to predicted defect bands for each specimen type; individual pores as superimposed '*z*' projections to a single plane (insets) allows for simple visualisation of defects in the *x-y* plane. Note that the figures are best viewed in colour.

3.2. Fatigue characteristics of specimen types

Figure 4 shows the number of cycles to failure for each of the specimen types. The red error bars indicate the 95% confidence interval of ±2σ around the mean for each set. Based on this confidence interval, one obvious outlier is identified (*see* blue arrow), whose number of cycles to failure statistically differs from the other results and is hence removed from the statistical analysis presented forthwith.

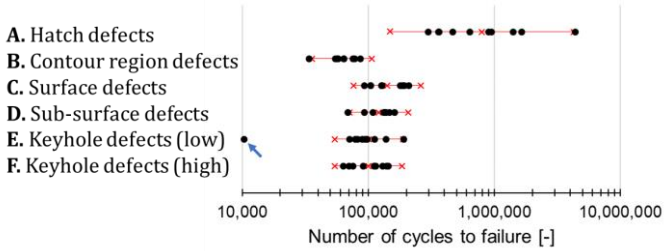

Figure 4. Dramatic differences in the fatigue life of specimens is observed, where hatch defects give superior life expectancy, keyhole defects lead to moderate results and lack-of-fusion defects are detrimental.

As shown in Figure 4, specimen type A in which only standard 'as-built' hatch defects are present performed best with an average of almost 800,000 cycles to failure and almost six times better than the runner up type C. This can be attributed to the relatively low number of defects, and low average defect size and volume. Specimen types C, D, E & F show similar fatigue performance with an average life between 100,000 and 140,000 cycles. A high number of defects near the specimen edge or mostly in the core region does not result in a significant difference in life expectancy. The fact that defects are generally spherical can be an explanation for the longer life compared to specimen type B in which angular and sharper notch type defects likely serve to accelerate the fatigue failure. Stress concentrations near edges of the irregularly shaped defects are known from classical understanding to be particularly detrimental in cyclic loading scenarios. This is also observed in the results of specimen type B, which gave the lowest average number of cycles to failure of just above 60,000 cycles.

3.3. Correlating fatigue characteristics of specimens

Key parameters that contribute to the fatigue life are the size, shape and location of the *killer* defect, i.e. the defect from which the crack initiated that failed the specimen. Figure 5 correlates the size of the killer defect to the fatigue life performance of the specimen types. Important to realize is that in this case the maximum defect size is determined after each failure, whereas the afore defect sizes were detected by XCT analysis of one specimen of each type prior to fatigue testing. A summary of XCT-detected defect sizes and volumes is listed in Table 2.

As shown in Figure 5, smaller defect sizes in general lead to longer life. Killer defects related to hatch scanning (specimen type A) generally do not extend beyond 200 µm leading to significantly longer fatigue life compared to the other specimen types. Although XCT revealed a larger maximum defect size of 260 µm, such large defects do not necessarily lead to a killer defect. Inset I shows the best performing specimen, in which case failure initiated at the surface near a spherical defect of 100 µm.

Specimen types C, D, E & F exhibit an equally sized killer defect, generally between 200 µm and 400 µm, which is comparable to the XCT-detected maximum defect sizes. Although fatigue performance is similar, specimen type C, in which surface defects were intentionally implemented, exhibited larger killer defect

sizes. Similarly, XCT analysis also showed the largest defect sizes and volumes for type C. This however did not lead to a worse fatigue performance compared to types D, E & F. The aforementioned outlier is shown in inset II. Two killer defects both about 300 µm within one *x-y* cross section were observed leading to a stress amplification and hence extremely low fatigue performance. Finally, similar to XCT analysis, specimen type B shows the largest killer defect sizes extending up to 1 mm in size and cause of the poor fatigue performance. This is shown in particular in inset III, showing a 1 mm lack-of-fusion defect that includes unmolten powder particles as well.

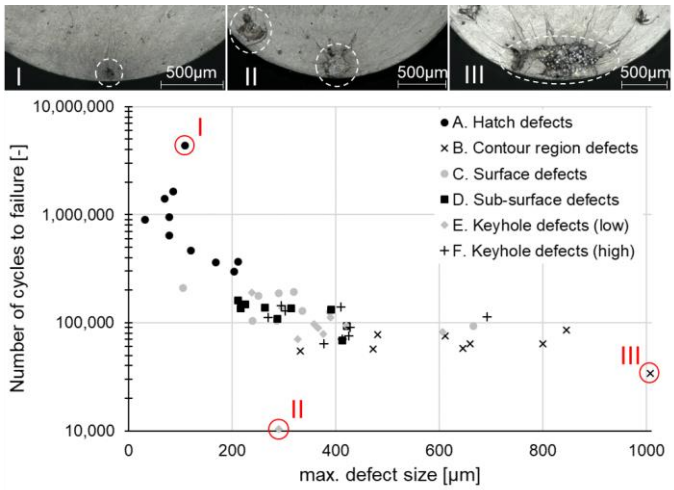

Figure 5. Smaller defect sizes generally lead to longer life. Through analysis of failure surfaces (insets), killer defect position is in 79% nearest the outer surface of specimens.

Next to defect size and shape, proximity to the outer surface is also known to be detrimental to fatigue resistance [15]. Examination of the killer defect location on the failure surfaces confirmed this. 79% of the specimen tested failed due to a defect at the outer surface. The remaining 21% failed from defects observed at a sub-surface location. In these cases, the average distance to the edge was 22.8 µm. Specimen types A & B failed in all but one case from the surface. Also for the dense keyhole-dominated defects in the core of specimen types E & F, 74% of the failures emanated from the surface, confirming the need of post-process surface finishing of AM components.

Table 2. Summary of XCT image analysis listing detected pore count, and defect sizes and volumes for each specimen type.

Specimen type	Pore count [-]	Avg. defect size [µm]	Max. defect size [µm]	Avg. defect volume [mm³]
A. Hatch defects	149	79	260	$7.1 \cdot 10^{-05}$
B. Contour region defects	631	111	729	$2.7 \cdot 10^{-04}$
C. Surface defects	1325	119	409	$1.8 \cdot 10^{-04}$
D. Sub-surface defects	1072	75	215	$1.1 \cdot 10^{-04}$
E. Keyhole defects (low)	1376	69	336	$8.1 \cdot 10^{-05}$
F. Keyhole defects (high)	614	95	280	$1.1 \cdot 10^{-04}$

Next to defect size, shape and position, the material microstructure in proximity of the killer defect is known to play a role in crack initiation as well. The effect of thermal history on the microstructure in proximity of the killer defect has however not been analysed in this study.

A last set of 21 test specimens was tested at lower and higher stress levels. At lower stress levels (i.e. 100 MPa), the average fatigue life extended close to two million cycles for specimen types C, D, E & F. Type B also performed the poorest at this stress level (<800,000 cycles). Finally, at 197 MPa the average fatigue life of specimen type A was around 54,000 cycles, but with an average killer defect size of 152 µm remaining in line with results at lower stress levels.

4. Conclusions

Fatigue testing was conducted on LPBF specimens with varying laser scan strategies to understand the role of this in enhancing the integrity of LPBF components. In creating these geometries, it was shown that porosity distributions are highly dependent on the scan strategy and these can be manipulated to locate defects in less sensitive regions within the part. In this case, where fatigue life is particularly reduced by near-surface defects, by ensuring defects are closer to the core of the specimen.

The findings of this work provide preliminary guidance for 'material on' considerations for manufacturing chains including AM. It is apparent that where superior surface integrity is sought the regions associated with adjacent skin passes, locations where skin and hatch scans meet, and laser turn points are likely to contain defects, and as such should be removed by machining operations. While LPBF processes continue to develop it should be expected that integrity will improve but it is also apparent that careful process planning along the entire manufacturing chain is required for fatigue applications.

References

[1] La Monaca, A., Murray, J.W., Liao, Z., Speidel, A., Robles-Linares, J.A., Axinte, D.A., Hardy, M.C., Clare, A.T., 2021, Surface integrity in metal machining - Part II: Functional performance, International Journal of Machine Tools and Manufacture, 164:103718.

[2] Everton, S.K., Hirsch, M., Stravroulakis, P., Leach, R.K., Clare, A.T., 2016, Review of in-situ process monitoring and in-situ metrology for metal additive manufacturing, Materials & Design, 95:431-445.

[3] De Chiffre, L., Carmignato, S., Kruth, J.P., Schmitt, R., Weckenmann, A., 2014, Industrial applications of computed tomography, CIRP Annals, 63(2):655-677.

[4] Maskery, I., Aboulkhair, N.T., Corfield, M.R., Tuck, C., Clare, A.T., Leach, R.K., Wildman, R.D., Ashcroft, I.A., Hague, R.J.M., 2016, Quantification and characterisation of porosity in selectively laser melted Al–Si10–Mg using X-ray computed tomography, Materials Characterization, 111:193-204.

[5] Leach, R.K., Bourell, D., Carmignato, S., Donmez, A., Senin, N., Dewulf, W., 2019, Geometrical metrology for metal additive manufacturing, CIRP Annals, 68(2):677-700.

[6] Wits, W.W., Carmignato, S., Zanini, F., Vaneker, T.H.J., 2016, Porosity testing methods for the quality assessment of selective laser melted parts, CIRP Annals, 65(1):201-204.

[7] Du Plessis, A., Razavi, S.M.J., Wan, D., Berto, F., Imdaadulah, A., Beamer, C., Shipley, J., MacDonald, E., 2022, Fatigue performance of shelled additively manufactured parts subjected to hot isostatic pressing, Additive Manufacturing, 51:102607.

[8] Xu, Z., Dunleavey, J., Antar, M., Hood, R., Soo, S.L., Kucukturk, G., Hyde, C.J., Clare, A.T., 2018, The influence of shot peening on the fatigue response of Ti-6Al-4V surfaces subject to different machining processes. International Journal of Fatigue, 111:196-207.

[9] Kruth, J.P., Levy, G., Klocke, F., Childs, T.H.C., 2007, Consolidation phenomena in laser and powder-bed based layered manufacturing, CIRP Annals, 56(2):730-759.

[10] Romano, S., Brückner-Foit, A., Brandão, A., Gumpinger, J., Ghidini, T., Beretta, S., 2018, Fatigue properties of AlSi10Mg obtained by additive manufacturing: Defect-based modelling and prediction of fatigue strength, Engineering Fracture Mechanics, 187:165-189.

[11] Bourell, D., Kruth, J.P., Leu, M., Levy, G., Rosen, D., Beese, A.M., Clare, A.T., 2017, Materials for additive manufacturing, CIRP Annals, 66(2):659-681.

[12] Beevers, E., Brandão, A.D., Gumpinger, J., Gschweitl, M., Seyfert, C., Hofbauer, P., Rohr, T., Ghidini, T., 2018, Fatigue properties and material characteristics of additively manufactured AlSi10Mg – Effect of the contour parameter on the microstructure, density, residual stress, roughness and mechanical properties, International Journal of Fatigue, 117:148-162.

[13] Doube, M., 2021, Multithreaded two-pass connected components labelling and particle analysis in ImageJ, Royal Society Open Science, 8(3):201784.

[14] Martin, A.A., Calta, N.P., Khairallah, S.A., Wang, J., Depond, P.J., Fong, A.Y., Thampy, V., Guss, G.M., Kiss, A.M., Stone, K.H., Tassone, C.J., Nelson Weker, J., Toney, M.F., Van Buuren, T., Matthews, M.J., 2019, Dynamics of pore formation during laser powder bed fusion additive manufacturing, Nature Communications, 10(1):1987.

[15] Yadollahi, A., Shamsaei, N., 2017, Additive manufacturing of fatigue resistant materials: Challenges and opportunities, International Journal of Fatigue, 98:14-31.